Bifurcation analysis of a two-delay model for the Atlantic Meridional Overturning Circulation

Renzo Mancini[1], Stefan Ruschel[2], Henk A. Dijkstra[3]
and Bernd Krauskopf[1]

[1]Department of Mathematics, The University of Auckland, Private Bag 92019, Auckland 1142, New Zealand

[2]School of Mathematics, University of Leeds, Woodhouse Lane, Leeds LS2 9JT, United Kingdom

[3]Institute for Marine and Atmospheric Research Utrecht, Utrecht University, Princetonplein 5, 3584 CC Utrecht, The Netherlands

September 2025

Abstract

The Atlantic Meridional Overturning Circulation (AMOC) is a climate-relevant ocean current system responsible for the meridional heat transport in the Atlantic. The AMOC strength is affected by a meridional density difference, where the density in the northern North Atlantic is controlled by an advective and a convective feedback. Here, we introduce and study a conceptual mathematical model of the variability of the AMOC strength by representing these feedbacks as delayed terms in a scalar delay differential equation (DDE) for the salinity in the northern North Atlantic. After scaling and without external input, this DDE has the associated delay times τ and σ as its only parameters. We perform a numerical bifurcation analysis of this deceptively simple-looking DDE AMOC model with the continuation software package DDE-Biftool. We find and characterize intricate dynamical regimes, including those exhibiting complicated oscillations associated with homoclinic connections. These results are presented as bifurcation diagrams in the (τ, σ)-plane, where we identify a codimension-two Belyakov transition as an organising center for nearby complicated dynamics. Moreover, we present a detailed analysis of different attractor regions in the (τ, σ)-plane, which we identify by computing the (strong) unstable manifold of a physically relevant equilibrium. As a general picture, we find that attractor regions repeat as the values of either σ or τ increase, including in physically relevant regions of these two (scaled) delay times. In this way, we clarify where different types of dynamics — such as periodic orbits of different periods, invariant tori, and chaotic dynamics — can be observed, and how they emerge or disappear.

1 Introduction

The Atlantic Ocean Circulation is dominated by several large-scale currents, one prominent example being the Gulf Stream. The depth-dependent northward and southward volume transport of these currents is the Atlantic Meridional Overturning Circulation (AMOC). The AMOC is responsible for the northward heat transport which affects climate around the Atlantic basin [6]. The strength of the AMOC plays an essential role for the overall global climate [36, 44], and its variability has been directly linked with different climate phenomena, including the Sahel drought [37], variability in Amazon rainfall [15], changes in the climate of the North American continent [45], and the frequency of Atlantic hurricanes [47].

In the northern regions of the Atlantic, warm surface water from the upper branch of the AMOC is cooled and transformed into water of the deep AMOC branch. One of the regions where this water mass transformation occurs is the Subpolar Gyre (SPG) region. Key components of the SPG region are currents in the Labrador and Irminger Seas, generating an overall counterclockwise surface flow and the transformation of large volumes of lighter surface waters to denser deep waters in the interior of these seas. Convective mixing due to negative surface buoyancy input (e.g., heavy water over light water) is a key aspect of this water mass transformation process [31]. A hierarchy of models is available for studying aspects of the AMOC, from conceptual models with only a few degrees of freedom to Earth System Models (ESMs) having billions of degrees of freedom [11]. From a mathematical perspective, ESMs and other large-scale models are challenging to analyze due to their very large number of variables and parameters. We are concerned here with conceptual climate models at the other end of the scale. These much 'simpler' models attempt to capture certain key aspects of the system while being amenable to mathematical analysis.

A typical category of such conceptual models are box models, where spatial averages of relevant observables are considered, such as temperature and salinity, which are coupled through transport processes. The most prominent example of such an AMOC model is the Stommel [42] two-box model, where the boxes represent equatorial and polar volumes. This model showed that multiple equilibria of the AMOC can exist, and it identified a positive feedback, the salt-advection feedback, involved in the transition from a strong to a weak AMOC state. An increase in the strength of the AMOC enhances the salinity transported northward, which increases the density in the polar box and, hence, further strengthens the AMOC, creating a positive feedback loop. Welander [48] later found that convective processes, arising from static instability, can also lead to multiple equilibria of the AMOC. The underlying feedback is a convective one: when a salinity perturbation is added to the upper layer of a non-convecting state, convection can occur. This mixing with saltier water from below increases the density of the upper layer, sustaining convection.

In Sec. 2, we introduce a conceptual model of the AMOC based on representing these feedbacks as delayed terms, resulting in a delay differential equation (DDE) of the form

$$x'(t) = x(t-\tau)(1-x(t-\sigma)), \tag{1}$$

after scaling in the absence of external forcing. Here, the prime denotes derivation with respect to time, and τ and σ represent time delays associated with the advective and convective feedbacks, respectively. Equation (1) is our central object of study, and we also refer to it as the (unforced) North Atlantic Salinity Two Feedback (NAS2F). It looks deceptively simple with the two (rescaled) delay times τ and σ as the only parameters. Other systems with two feedback loops can be found in many application areas, including climate dynamics [17, 26, 27], but typically the delayed feedback terms contribute additively. An important and novel feature of the NAS2F model is that the two delay loops interact in a *multiplicative* way, rather than as a sum. Because of this property, Eq. (1) has relevance beyond climate modeling as a special DDE: it is a generalisation of the delayed logistic equation with two independent delays. In fact, the case $\tau = \sigma$ of equal delays has arisen in the modeling of cancer, for example, to describe the growth of cancer in a female mouse's body [38], and as a way to take the cell cycle into account in tumor dynamics [34].

From a more mathematical point of view, Eq. (1) is of great relevance since it is a generalization of a classic DDE, the so-called Hutchinson-Wright equation for which $\tau = 0$ so that σ is the only delay. This specific DDE has been studied in various contexts, motivated by two seminal papers concerning areas as diverse as the distribution of primes [49] and population dynamics [23]. The Hutchinson-Wright equation is strongly connected to the development of the theory of DDEs; it is one of the first examples highlighting the nature of solutions of DDEs in comparison to their ODE counterparts. A two-delay version of the Hutchinson-Wright equation has been considered, where the second term of the logistic equation features the sum of two linear terms with different delays [5, 30, 33]. The form of Eq. (1) with two independent delays in each of the two terms of the logistic equation, however, has not been analysed to the best of our knowledge. This fact provides further motivation for the bifurcation study of the NAS2F model presented here, beyond its relevance for investigating the interplay between feedback mechanisms in the AMOC.

We provide here an exploration and in-depth analysis of the dynamics exhibited by the NAS2F model (1), effectively for any choices of the two independent parameters τ and σ. Section 2 provides further information on the NAS2F model and its rescaling. Section 3 presents a bifurcation study for smaller to intermediate values of the two delays. We begin in Sec. 3.1 with the stability analysis of the two equilibrium solutions $\mathbf{0}$ and $\mathbf{1}$; they represent (scaled) constant-salinity solutions, and the boldface type setting distinguishes them from the numbers 0 and 1. The stability analysis reveals a 'checkerboard' grid pattern of Hopf bifurcations, and we proceed in Sec. 3.2 by considering the emerging periodic solutions and their disappearance in Shilnikov homoclinic bifurcations. A two-parameter bifurcation study in Sec. 3.3 then shows the emergence of more complicated dynamics and associated further bifurcations due to a transition, known as a Belyakov point, where the Shilnikov homoclinic orbit changes from 'tame' to 'wild'.

Section 4 then focuses on where in the (τ, σ)-plane one finds attractors of Eq. (1), including in parameter ranges of small σ and large τ, which carry physical relevance. To this end, we employ a suitable strategy for sampling physically relevant initial conditions; specifically, we determine where the one-dimensional unstable manifold of the equilibrium $\mathbf{0}$ ends up. This approach reveals a repeating structure of attractor regions of the NAS2F model, which we then characterize further in terms of how they are bounded and which types of attractors can be found. We first consider in Sec. 4.1 the main and largest attractor region found for lower values of τ and σ. It is bounded by bifurcations we identified in Sec. 3.3, specifically by curves of Hopf bifurcation below and of homoclinic bifurcation above, and we show that there is a sizable subregion with chaotic behaviour. For increasing σ we find a repeating sequence of further attractor regions for lower values of τ that are bounded below and above by further curves of homoclinic bifurcations. Notably, these curves and attractor regions accumulate on the σ-axis, as we show in Sec. 4.2. The associated complicated dynamics cannot be observed for the Hutchinson-Wright equation with $\tau = 0$, but it 'emerges' as soon as the second delay τ is 'switched on'. Section 4.3 then shows that there is also a sequence of attractor regions for increasing τ. These regions turn out to be bounded by curves of torus bifurcation, with associated resonance phenomena and a considerable level of multistability between different types of attractors. Our estimates show that these attractor regions exist within ranges of larger τ and smaller σ that are physically plausible in the context of AMOC dynamcis.

The final Sec. 5 provides a brief discussion of our results and an outlook with the emphasis on directions for future research within the context of AMOC dynamics.

2 Formulation of the NAS2F model

The advective and convective feedbacks, which are represented in a very elementary way in box models [42, 48], in reality are due to a set of complex processes involving the three-dimensional ocean circulation, deep water formation processes and sea-ice influences [46]. These processes inherently feature a delay between cause and effect; here the cause is a change in the salinity (or density) in the northern North Atlantic. This gives a delayed effect, either through the advective feedback (with a delay τ_{phys}) or through the convective feedback (with a delay σ_{phys}), on the salinity of the northern box.

This view motivates our model, shown schematically in Fig. 1. Panel (a) shows a latitudinal

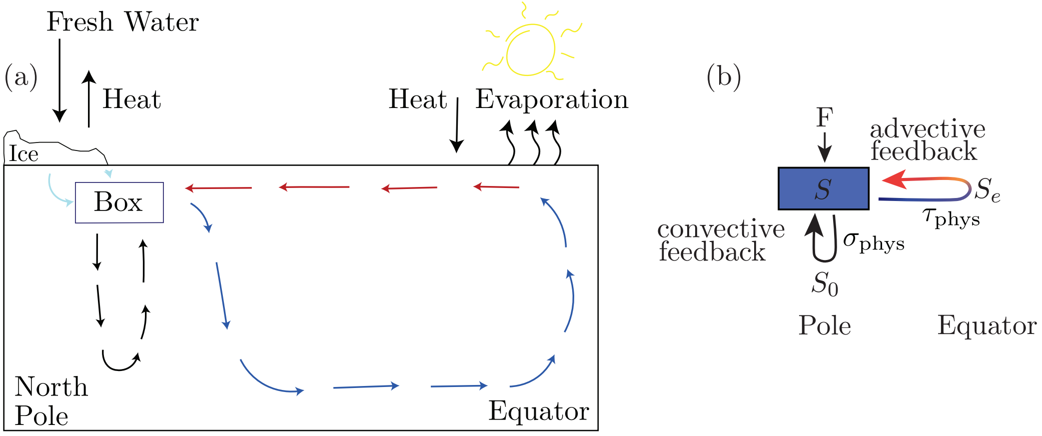

Figure 1: Schematic diagram of the NAS2F model. Panel (a) is a representation of the two main feedback loops of the North Atlantic gyre, and panel (b) shows the box model diagram corresponding to the (unscaled) Eq. (2). The salinity S in the polar surface box is subject to two feedback loops with delays $\tau_{\rm phys}$ and $\sigma_{\rm phys}$, where S_e is a typical salinity in the equatorial region, S_0 is a global mean salinity and F represents an external freshwater flux forcing.

profile of the North Atlantic Ocean, from the Polar regions on the left to the Equatorial regions on the right. The box located at the surface near the Pole is subject to the advective feedback loop and the convective feedback loop. Panel (b) shows a simpler sketch of the box, which is characterized by its salinity S, with its two feedback loops with constant equatorial salinities S_e at the Equator and a global average salinity S_0, and the associated time delays $\tau_{\rm phys}$ and $\sigma_{\rm phys}$. A surface freshwater flux is modeled by an external forcing F. Modeling the AMOC in this conceptual way rests on the idea of reducing the the complicated processes that give rise to the two main feedback loops by describing them by terms with explicit delay times as parameters [4, 24].

This explicit modeling approach allows one to concentrate on the effect of key physical feedback loops on the AMOC by formulating a model in the form of a DDE, which is amenable to mathematical analysis with advanced tools from dynamical systems and bifurcation theory; for other examples of DDE climate models, see [14, 24, 27]. In this approach, the advective exchange function is represented as $Q = \Psi S(t-\tau)/S_0$, where Ψ is a transport coefficient and the AMOC strength is given by QV where V is a typical volume of a sector in the northern North Atlantic [8]. The advective salinity transport is then given by $Q(S_e - S(t-\sigma_{\rm phys}))$, where S_e is the equatorial salinity and the delay σ is representing the effects of the convective feedback. This then leads to the overall DDE, which we call the *North Atlantic Salinity Two Feedback (NAS2F) model*, decribing the evolution of surface salinity S, *i.e.*

$$\frac{dS(t)}{dt} = \frac{\Psi}{S_0} S(t-\tau_{\rm phys})(S_e - S(t-\sigma_{\rm phys})) + F. \tag{2}$$

Note that the delay terms are multiplied due to the advective nonlinearity of the salinity transport; here, the delays, $\tau_{\rm phys}$ of the advective and $\sigma_{\rm phys}$ of the convective feedback loop, are 'physical' parameters expressed in terms of years. The last term of (2) models an external surface freshwater flux, represented as a virtual salinity flux of strength F.

The NAS2F (2) is a scalar DDE for the salinity S with the two time delays $\tau_{\rm phys}$ and $\sigma_{\rm phys}$. As such, it is an effective conceptual model for studying the temporal evolution of the surface water salinity in the Northern-most Atlantic Ocean, subject to the two main feedback loops observed in the AMOC's North Atlantic gyre: the advective Pole-Equator feedback loop with

τ_{phys} representing the (average) return time of water masses transported by ocean currents, and the convective loop with σ_{phys} representing the (average) mixing time between surface and deep water near the Pole. The advantage of Eq. (2) is that the influence of the delay times on the observed behaviour can be studied explicitely. The 'price' one pays over other box models in the form of ordinary differential equations (ODEs) without delay terms is that a DDE is an infinite dimensional system: namely, it requires as initial condition a history segment back to the longest delay time [12, 21, 22, 41]. In the case of Eq. (1), this corresponds to prescribing $S(t)$ over the length of the longer of the two feedback, either τ_{phys} or σ_{phys}; and, correspondingly, for $x(t)$ in Eq. (1). The other side of the coin is that, as an infinite-dimensional dynamical system, the NAS2F has the capacity to exhibit complex dynamical behaviour, despite being a scalar model.

In this paper, we consider the NAS2F model (2) for the case that there is no forcing ($F = 0$), which allows the study of the pure interaction between the two main AMOC feedback loops. Realizing that Eq. (2) with $F = 0$ has the two equilibrium solutions $S \equiv 0$ and $S \equiv S_e$, we apply the rescaling

$$x(t) = \frac{S(t)}{S_e}, \ \tau = \frac{\Psi S_e}{S_0}\tau_{\text{phys}}, \ \sigma = \frac{\Psi S_e}{S_0}\sigma_{\text{phys}}, \ \tilde{t} = \frac{\Psi S_e}{S_0}t, \tag{3}$$

to obtain the dimensionless form Eq. (1) presented in the introduction. Here, the prime denotes derivation with respect to the rescaled time $\tilde{t}$; however, for notational convenience, we drop the tilde and refer to the rescaled time in Eq. (1) again simply as t from now on.

Ranges of values for the (rescaled) parameters τ and σ can be obtained as follows. First, the range of equatorial salinities is $S_e \in [34.5, 36.5]$ psu and $S_0 = 35$ psu (based on ORAS5 data since 1985 and the World Ocean Atlas 1994 [29]). Second, using a typical northern box volume $V = 5 \times 10^{16}$ m^3 (*e.g.*, for a sector $40 - 60$°N in the Atlantic with a depth of 4×10^3 m) and an AMOC strength of $10 - 20$ Sv, the value of the main scaling factor lies in the range $\Psi/S_0 \in [2, 4] \times 10^{-10}$ s^{-1}. Third, the physical delay times τ_{phys} and σ_{phys} can be estimated by the time it takes for the salinity to advance over the advective and convective feedback loop, respectively. The advective time scale depends on the transport of salinity over the overturning loop and, hence, on the latitude the deeper water upwells to the surface; a rough estimate gives the range $\tau_{\text{phys}} \in [10 - 100]$ years. While the convective mixing process is practically instantaneous (a few days), the delay time scale is determined by adjustment through restratification and subsequent response of the subpolar gyre. This entire process can take up to a decade, so a rough estimate is $\sigma_{\text{phys}} \in [0.4 - 10]$ years. With the scaling (3), this then leads to the ranges $\tau \in [5, 50]$ and $\sigma \in [0.2, 5]$ for the parameters τ and σ of Eq. (1); note that the advective delay time τ is much larger than the convective delay time σ.

3 Bifurcation analysis of the NAS2F model

The theory on DDEs with constant delays is well developed and can be found in standard textbooks, such as [12, 22]. In particular, the bifurcation theory of constant-delay DDEs is effectively analogous to that for ODEs — in the sense that qualitative changes are mediated by finite-dimensional bifurcation equations in well defined finite dimensional center manifolds [21]. Moreover, just like for ODEs, advanced numerical tools from bifurcation theory are available for DDEs; they allow one to find and follow or continue solutions in parameters while monitoring their stability to identify bifurcations. We use here the package DDE-Biftool [13, 40] to detect and continue equilibria and periodic orbits of Eq. (1), as well as their codimension-one bifurcations and even certain connecting orbits. Additionally, DDE-Biftool is able to compute normal form coefficients, which allows us to identify codimension-two bifurcations on bifurcation curves in the (τ, σ)-plane.

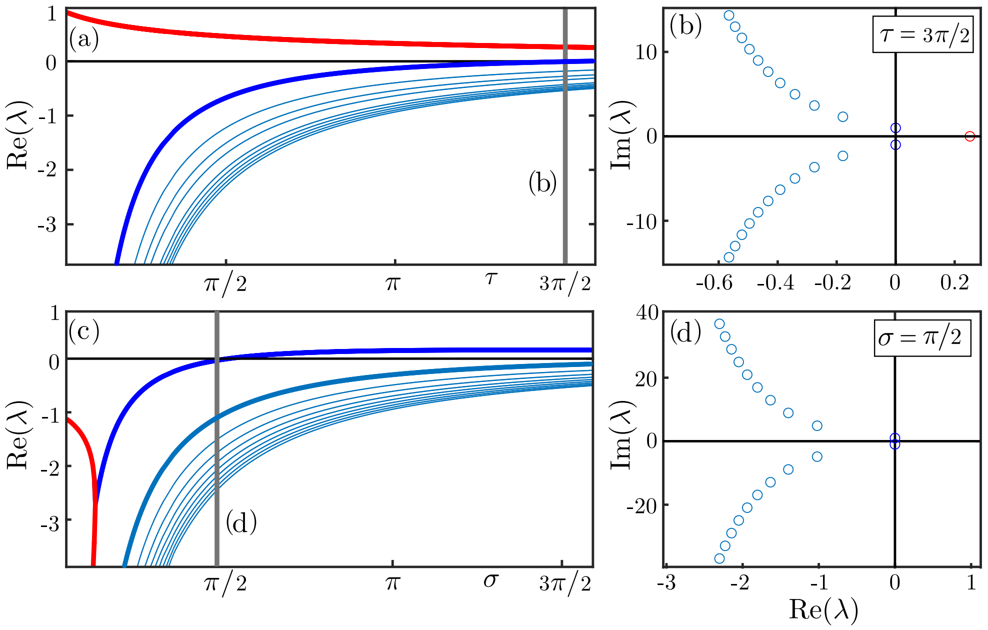

Figure 2: The spectra of the equilibria of Eq. (1). Panels (a) and (c) show the eigenvalues with the ten largest real parts of **0** and of **1**, respectively; here, real eigenvalues are shown in red, and the leading one of the complex pairs (blue) are bold. The spectrum at the respective first Hopf bifurcation (vertical grey lines) is shown in panels (b) and (d).

3.1 Stability of equilibria and the grid of Hopf bifurcations

The steady states of Eq. (1) are the constant solutions **0** and **1**, and their location and existence do not depend on the parameters τ and σ. Hence, there are no saddle-node bifurcation (of equilibria) but the stability of the equilibria **0** and **1** may change at Hopf bifurcations. The stability of an equilibrium of a DDE is determined by its linearization, which involves taking derivatives both of the instantaneous and of each delayed term, yielding an extended Jacobian and associated characteristic equation. The latter is a transcendental equation with exponential terms, which implies the existence of infinitely many eigenvalues. For constant-delay DDEs, all eigenvalues are discrete and infinitely many of them are in the left half of the complex plane [12, 21, 22, 41]. For the specific case of Eq. (1), the characteristic equation decouples, giving

$$-\lambda + e^{-\lambda\tau} \text{ at equilibrium } \mathbf{0}, \text{ and} \tag{4}$$

$$-\lambda - e^{-\lambda\sigma} \text{ at equilibrium } \mathbf{1}. \tag{5}$$

These are, in fact, the characteristic equations for the simplest case of a linear DDE with positive and negative feedback, respectively, and the associated spectra are well known from the standard theory [21, 41].

It follows from (4) that **0** has a unique real eigenvalue $\lambda_0 = \frac{1}{\tau} W_0(\tau) > 0$ in the right half-plane, where W_0 is the fundamental branch of the Lambert W function; all other eigenvalues are complex conjugate pairs that initially have negative real parts. For increasing τ, complex pairs cross the imaginary axis one-by-one at

$$\tau = \frac{3\pi}{2} + 2(n-1)\pi, \ n \in \mathbb{N}, \tag{6}$$

which are Hopf bifurcations of **0** we refer to as H_τ^n. Similarly, it follows from (5) that **1** has two

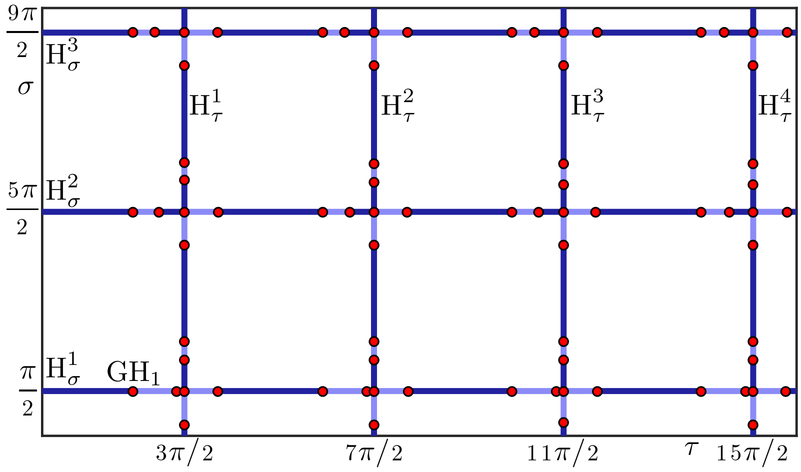

Figure 3: The grid in the (τ, σ)-plane of Eq. (1) of the Hopf bifurcations H_τ^n of $\mathbf{0}$ and H_σ^n of $\mathbf{1}$. The respective Hopf bifurcation is supercritical when dark blue and subcritical when light blue; red dots represent changes of criticality at points of generalised Hopf bifurcation, and the first such point on H_σ^1 is labelled GH_1.

distinct negative real solutions for small σ, which become a complex pair at $\sigma = e^{-1}$; all other eigenvalues are complex conjugate pairs with negative real parts for small σ. For increasing σ, complex pairs cross the imaginary axis one-by-one at

$$\sigma = \frac{\pi}{2} + 2(n-1)\pi, \ n \in \mathbb{N}, \tag{7}$$

which are Hopf bifurcations of $\mathbf{1}$ we refer to as H_σ^n. In particular, $\mathbf{1}$ is stable up to H_σ^1, that is, for $0 \leq \sigma < \frac{\pi}{2}$.

Figure 2 illustrates these two spectra by showing the eigenvalues with the ten largest real parts. Panels (a) and (c) shows how the eigenvalues of $\mathbf{0}$ and $\mathbf{1}$ depend on τ and σ, respectively, and panels (b) and (d) show the spectrum at the corresponding first two Hopf bifurcations H_τ^1 and H_σ^1. While the eigenvalues and associated changes of stability can be found analytically from Eqs. (6) and (7), we computed them with the package DDE-Biftool. This has the advantage that the normal form (Lyapunov) coefficient determining the criticality of the Hopf bifurcation is found as well, which is a difficult task to achieve analytically.

Figure 3 shows the (τ, σ)-plane with the Hopf bifurcation curves H_τ^n and H_σ^n. In accordance with Eqs. (6) and (7), they form a grid of vertical and horizontal lines at distance 2π in both τ and σ. We remark that the intersection points are not codimension-two points of Hopf-Hopf bifurcation, because each Hopf bifurcation takes place at a different equilibrium. We distinguish in Fig. 3 the segments where the Hopf bifurcation is supercritical and subcritical. Changes of criticality occur at codimension-two generalized Hopf (GH) bifurcation points; they have been found with DDE-Biftool, and the first such point on H_σ^1 is labelled. When the Hopf bifurcation is supercritical and the bifurcating equilibrium is attracting, then the emerging periodic orbit is stable. This happens only along the supercritical segments of the horizontal line H_σ^1; along all other lines and segments, the bifurcating periodic orbit is of saddle type.

A conclusion from Fig. 3 is that an attracting periodic orbit emerges when σ is increased through H_σ^1 for τ to the left of the point GH_1. This is illustrated in Fig. 4 for the case $\tau = 0$, that is, for the Hopf bifurcation of the logistic equation with a single delay [16] — the well-studied case of the Hutchinson-Wright equation [23, 49]. More specifically, we show here time series of (1) obtained by integration from the initial condition $x \equiv 0.5$ with the Python package *Pydelay*, which employs an algorithm based on the Bogacki-Shampine method [3].

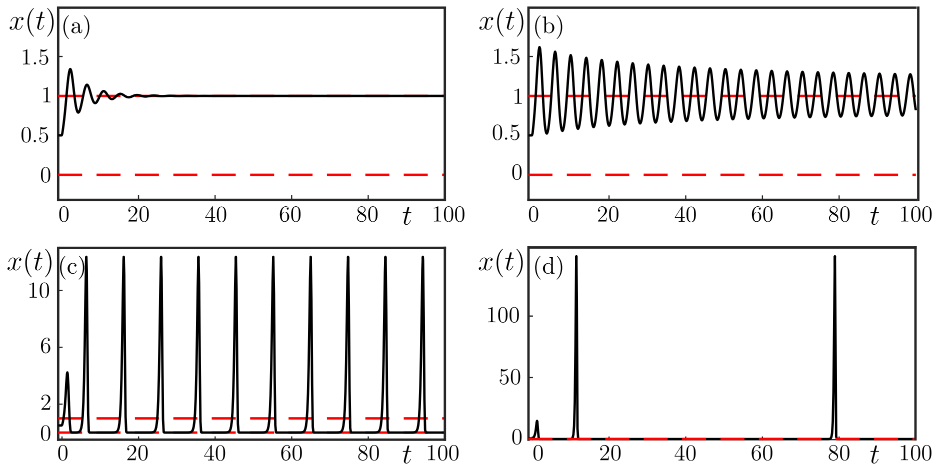

Figure 4: Time series of (1) with $\tau = 0$ for $\sigma = 1.2$ (a), $\sigma = 1.6$ (b), $\sigma = 3.5$ (c) and $\sigma = 6$ (d); obtained by integration from $x \equiv 0.5$.

For $\sigma < \pi/2$, below H_τ^1, the solution converges to the stable equilibrium $\mathbf{1}$ in an oscillatory fashion, as shown in Fig. 4(a) for $\sigma = 1.2$. For σ past the Hopf bifurcation H_σ^1 there is globally attracting periodic orbit, which is initially practically sinusoidal, as in panel (b) for $\sigma = 1.6$. As σ is increased, the attracting periodic orbit increases in amplitude and becomes pulse-like with distinguished spikes, as shown in panel (c) for $\sigma = 3.5$; notice here that there are segments very close to the equilibrium $\mathbf{0}$. When σ is increased further, as in panel (d) for $\sigma = 6$, the time the periodic orbit spends near $\mathbf{0}$ increases considerably and the amplitude of the spikes grows massively; notice the difference in scale between the panels.

3.2 Shilnikov homoclinic bifurcation of equilibrium 0

The increase of the time spent by the solution near $\mathbf{0}$ observed in Fig. 4(d) suggests the existence of a homoclinic bifurcation. However, for $\tau = 0$, the equilibrium $\mathbf{0}$ has the single unstable eigenvalue $\lambda = 1$, because the characteristic equation (4) reduces to a simple degree-one polynomial. Therefore, the eigenspace of $\mathbf{0}$ is of dimension one, and there cannot be a generic homoclinic orbit to this equilibrium in the Hutchinson-Wright equation.

For $\tau \neq 0$, however, there exists a homoclinic bifurcation to the saddle equilibrium $\mathbf{0}$, which we refer to as $\mathrm{Hom}_{\mathbf{0}}$, where the attracting periodic orbit bifurcating from the supercritical segments of H_σ^1 disappears as σ is increased. The corresponding curve in the (τ, σ)-plane is shown in Fig. 5 near the point GH_1 on H_σ^1 from Fig. 3; also shown are the curve H_τ^1 and the curve S of saddle-node of periodic orbits, which emerges from the generalized Hopf point GH_1 and turns sharply at a cusp point C. Since the spectrum of $\mathbf{0}$ has a complex conjugate pair as its leading eigenvalues for $\tau > 0$ according to Sec. 3.1 and Fig. 2(a), the connecting orbit along the curve $\mathrm{Hom}_{\mathbf{0}}$ is a Shilnikov homoclinic orbit: the one-dimensional unstable manifold $\mathrm{W}^u(\mathbf{0})$ returns to the equilibrium $\mathbf{0}$ in a spiraling fashion. Note that $\mathrm{Hom}_{\mathbf{0}}$ has the σ-axis as its asymptote for $\tau \to 0$, in accordance with the fact that there cannot be a homoclinic bifurcation to $\mathbf{0}$ when $\tau = 0$. For increasing τ, the curve $\mathrm{Hom}_{\mathbf{0}}$ has a minimum near $\pi/4$ and then ends at the codimension-two Shilnikov-Hopf point SH_τ^1 on the curve H_τ^1 of Hopf bifurcation of the equilibrium $\mathbf{0}$.

Notice from Fig. 2(a) that the negative real part of the leading pair of complex conjugate eigenvalues of $\mathbf{0}$ is much larger in modulus than the real unstable eigenvalue. Hence, their sum, known as the saddle quantity of $\mathbf{0}$, is negative, which means that the homoclinic orbit is attracting and the Shilnikov bifurcation along $\mathrm{Hom}_{\mathbf{0}}$ is 'tame' and creates a single periodic orbit

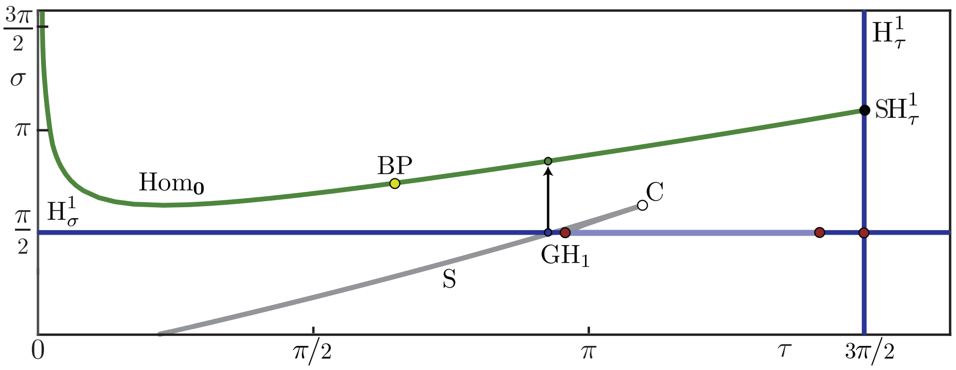

Figure 5: Bifurcation diagram in the (τ, σ)-plane of Eq. (1) near the point GH_1 with the curves H^1_σ and H^1_τ from Fig. 3; the curve S (grey) of saddle-node of periodic orbits, which emerges from GH_1 and has a cusp point C (white dot); and the curve $Hom_{\mathbf{0}}$ (green) of homoclinic bifurcation to $\mathbf{0}$, which has a the Belyakov point BP (ochre dot) at $(\tau, \sigma) \approx (1.97, 2.29)$ and ends at the Shilnikov-Hopf point SH^1_τ on H^1_τ. The arrow at $\tau = 2.9$ represents the branch of periodic solutions shown in Fig. 6.

[28, 39]. As τ is increased, however, the real part of the complex pair grows and the saddle quantity changes sign at $\tau \approx 1.97$; this point is known as a Belyakov point (BP) [2, 28], and it marks the transition of the Shilnikov homoclinic bifurcation along $Hom_{\mathbf{0}}$ to the 'wild' case, where the homoclinic orbit is repelling and complicated types of dynamics are created nearby [28, 39].

3.3 Further periodic orbits and their bifurcations near the wild Shilnikov bifurcation

Figure 6 illustrates the emergence of additional periodic orbits and Shilnikov bifurcations near the wild segment of the curve $Hom_{\mathbf{0}}$. Panel (a) and the enlargement panels (b) and (c) show the periodic orbit branch for $\tau = 2.9$ emerging from H^1_σ, as it approaches the homoclinic bifurcation $Hom_{\mathbf{0}}$ when σ is increased. This branch is represented here by its increasing period T. Panel (a) shows that it has a sequence of (pairs of) saddle-node bifurcations of periodic orbits S_j as it approaches the σ-value of the Shilnikov bifurcation in a characteristic oscillating fashion. The limiting Shilnikov homoclinic orbit on $Hom_{\mathbf{0}}$ is shown in Fig. 6(d) in projection onto the $(x(t-\tau), x(t))$-plane, illustrating how the unstable manifold $W^u(\mathbf{0})$ returns to $\mathbf{0}$ in a spiraling fashion to form the Shilnikov orbit. Near the points S_j one finds associated (pairs of) period-doubling bifurcation points PD_j on the branch, of which many are marked in panel (a). Low on the branch, for low values of T, one finds that the two points of a pair labelled PD_j are connected by a branch of period-two periodic orbits, on which one finds a further pair of period-doubling points that is connected by a branch of period-four periodic orbits, and so on. This is illustrated in the enlargement panel (b) of the corresponding frame in panel (a). However, Fig. 6(c) illustrates that branches of bifurcating periodic orbits do not connect in this way higher up the initial branch of periodic orbits. From the pair PD_4 onwards, one finds bifurcating branches of periodic orbits that oscillate as they approach a limiting σ-values for increasing period T, where they end on a particular Shilnikov bifurcation themselves. Panel (e) shows the limiting Shilnikov orbit of the branch of periodic orbits emerging from the point PD_4. Note that this period-two Shilnikov orbit is formed when $W^u(\mathbf{0})$ returns to near the equilibrium $\mathbf{0}$ but 'misses' and only connects to the equilirium upon the second return.

The identified bifurcation points can be continued as curves, and this results in the bifurcation

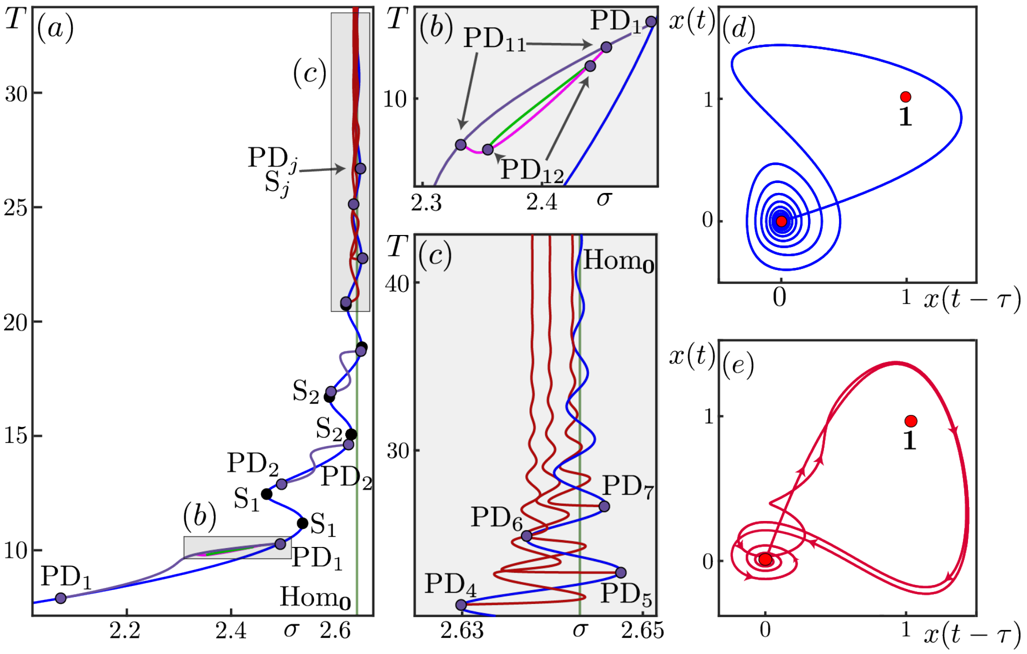

Figure 6: The branch of periodic orbits (blue) bifurcating from H^1_σ for $\tau = 2.9$ as it is continued in σ towards the wild Shilnikov homoclinic bifurcation at $\mathrm{Hom}_\mathbf{0}$, shown in terms of its period T in panel (a) and the enlargement panels (b) and (c), together with branches of periodic orbits (other colors) that emerge from points PD_j (purple dots) of period-doubling bifurcations near consecutive points S_j (black dots) of saddle-node bifurcations of periodic orbit S_j; the limiting σ-value is represented by a vertical grey line. Panel (d) shows the Shilnikov orbit on $\mathrm{Hom}_\mathbf{0}$, and panel (e) the nearby Shilnikov orbit to $\mathbf{0}$ that is approached by the branch emerging from PD_4 in panel (c), both in projection onto the $(x(t-\tau), x(t))$-plane.

diagram near the Belyakov point BP shown in Fig. 7(a). Since the different bifurcation curves accumulate quickly on $\mathrm{Hom}_\mathbf{0}$, we show them here in a relative plot: for each value of τ, we show the (signed) distance $\hat{\sigma}$ in σ of the respective curve from the corresponding point on $\mathrm{Hom}_\mathbf{0}$. In this representation in the $(\tau, \hat{\sigma})$-plane, the curve $\mathrm{Hom}_\mathbf{0}$ is the straight line with $\hat{\sigma} = 0$, and the Hopf bifurcation curve H^1_τ is a still vertical line (since it does not dependend on σ). The point BP indicates the beginning of the 'wild' section of $\mathrm{Hom}_\mathbf{0}$, and all shown bifurcation curves are to its right. Note that the pairs of points S_j and PD_j of the same label in Fig. 6(a) on either side of the limiting σ-value lie, in fact, on one and the same curve of the same label in the $(\tau, \hat{\sigma})$-plane of Fig. 7(a). The curves S_j have cusp points that approach the Belyakov point BP with increasing index j. Similarly, the curves PD_j have minima with respect to τ, which accumulate on BP for increasing j.

We identified further Shilnikov orbits as limits of period-two branches shown in Fig. 6(c), and computed them as curves $\mathrm{Hom}^k_\mathbf{0}$ that are also shown in the $(\tau, \hat{\sigma})$-plane of Fig. 7(a). These curves start and end at Shilnikov-Hopf bifurcation points on the curve H^1_τ, and they accumulate quickly with increasing index k to the 'wild' segment of $\mathrm{Hom}_\mathbf{0}$; each curve $\mathrm{Hom}^k_\mathbf{0}$ has a unique mimimum with respect to τ, and this sequence of minima converges to the Belyakov point BP. We remark that these Shilnikov orbits can be continued to the right of H^1_τ by the same boundary-value-problem setup for homoclinic orbits (as a strong connecting orbit of $\mathbf{0}$ to the small bifurcating periodic orbit of saddle type); for more details on the continuation of connecting orbits in DDE-Biftool see [13, 40]. In this way, we found the 'lowest' segment of the curve $\mathrm{Hom}^1_\mathbf{0}$ that spirals into the point labelled TP at $(\sigma, \tau) \approx (4.16, 3.14)$ in Fig. 7(a). This codimension-two point is known as a terminal point or T-point [7, 18, 20], and it lies on a curve $\mathrm{Hom}_\mathbf{1}$ of a homoclinic

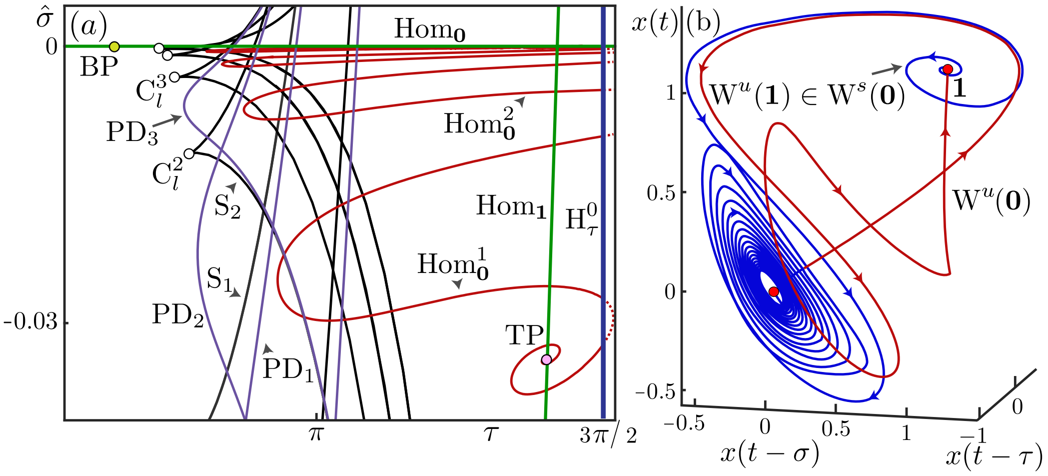

Figure 7: Bifurcation diagram in the rescaled $(\tau, \hat{\sigma})$-plane relative to the homoclinic bifurcation curve $\mathrm{Hom}_{\mathbf{0}}$, where $\hat{\sigma}$ is the (signed) σ-distance of a point to $\mathrm{Hom}_{\mathbf{0}}$. Panel (a) shows the curves $\mathrm{Hom}_{\mathbf{0}}$ of Shilnikov homoclinic orbit (green), H_τ^1 of Hopf bifurcation (blue), S_j of saddle-node bifurcations (black), PD_j of period-doubling bifurcations (purple), and $\mathrm{Hom}_{\mathbf{0}}^k$ of period-two homoclinic bifurcations (red). Also shown are the Belyakov point BP (ocre dot), cusp points C_j (white dots), and Shilnikov-Hopf bifurcation points (red dots). The curve $\mathrm{Hom}_{\mathbf{0}}^1$ ends at a T-point TP at $(\sigma, \tau) \approx (4.16, 3.14)$ (pink dot) on a curve $\mathrm{Hom}_{\mathbf{1}}$ (green) of homoclinic bifurcation to $\mathbf{1}$. Panel (b) shows the heteroclinic cycle at TP between the two equilibria $\mathbf{0}$ and $\mathbf{1}$.

bifurcation to the equilibrium $\mathbf{1}$, which we also computed and show.

The situation at the T-point is illustrated in Fig. 7(b) in projection onto $(x(t-\tau), x(t-\sigma), x(t))$-space: at TP, there exists a heteroclinic cycle between the two equilibria $\mathbf{0}$ and $\mathbf{1}$. It consists of the one-dimensional unstable manifold $\mathrm{W}^u(\mathbf{0})$, which lies in $\mathrm{W}^s(\mathbf{1})$ and, hence, connects to the saddle equilibrium $\mathbf{1}$. Note that this connecting orbit 'misses' the equilibrium $\mathbf{1}$ once and connects to it at the second approach; this phenomenon is inherited from the period-two homoclinic orbit $\mathrm{Hom}_{\mathbf{0}}^1$ in Fig. 6(e). We checked that the connecting orbit indeed spirals into $\mathbf{1}$ (due to its leading complex conjugate pair of stable eigenvalue); however, this spiralling is very 'steep' and, apart from a small overshoot, is not visible in Fig. 7(b). Simulataneously, at TP, the two-dimensional unstable manifold $\mathrm{W}^u(\mathbf{1})$ intersects $\mathrm{W}^s(\mathbf{0})$, creating the connecting orbit back to the saddle equilibrium $\mathbf{0}$ that is also shown in Fig. 7(b). A suitable perturbation of the overall heteroclinic cycle creates a homoclinic orbit to $\mathbf{1}$ as the intersection of $\mathrm{W}^u(\mathbf{1})$ and $\mathrm{W}^s(\mathbf{1})$; this happens along the curve $\mathrm{Hom}_{\mathbf{1}}$ in Fig. 7(a). We remark that the existence of a T-point implies complicated dynamics near it; specifically, the existence of further homoclinic and heteroclinic connections, of chaos, and of so-called α-flips [7, 10, 18, 20]. A more detailed discussion of the bifurcations close to the T-point TP is beyond the scope of this paper.

4 Attractor regions of the NAS2F model

We now turn to the question where in the (τ, σ)-plane observable attracting behaviour of Eq. (1) can be found. To this end, we identify the bounded attractor, if it exists, to which the one-dimensional unstable manifold $\mathrm{W}_1^u(\mathbf{0})$ converges. When the equilibrium $\mathbf{0}$ has a single real unstable eigenvalue then $\mathrm{W}_1^u(\mathbf{0}) = \mathrm{W}^u(\mathbf{0})$ is the one-dimensional unstable manifold of $\mathbf{0}$. According to Sec. 3.1, this is the case when $\tau < 3\pi/2$, and we refer to this part of the (τ, σ)-plane with smaller values of τ as Range I. However, the number of positive eigenvalues of $\mathbf{0}$ increases by two when pairs of complex conjugates eigenvalues cross the imaginary axis at the Hopf bi-

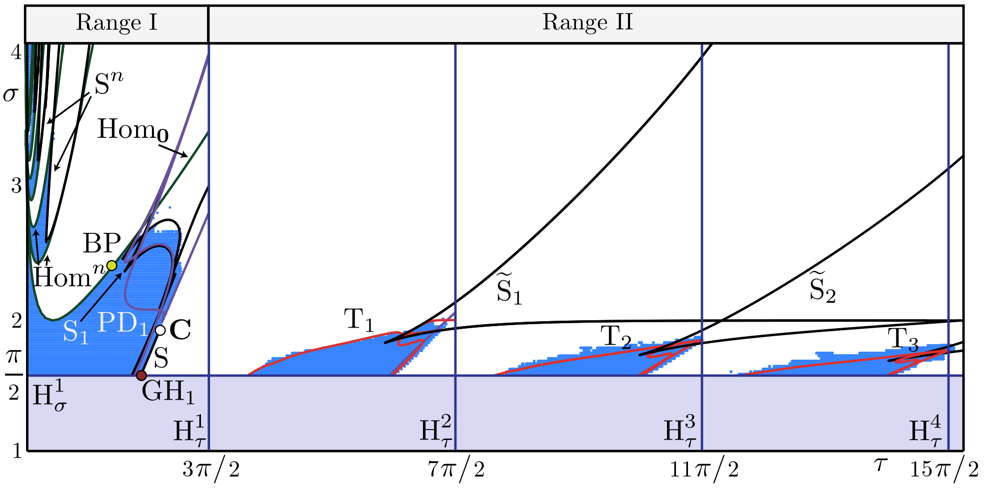

Figure 8: The (τ, σ)-plane of Eq. (1) with regions where the one-dimensional unstable manifold $\mathrm{W}^u_1(\mathbf{0})$ approaches an attractor, namely $\mathbf{0}$ in the light blue region and a different attractor in the dark blue regions. We distinguish Range I with $\tau < 3\pi/2$, where attractor regions are bounded by the bifurcation curves $\mathrm{Hom}_{\mathbf{0}}$, S, S_1, PD_1, Hom^n, and S^n, and Range II with $\tau > 3\pi/2$, where they are bounded by curves T_n of torus bifurcation and $\widetilde{\mathrm{S}}_n$ of saddle-node bifurcations.

furcations H^n_τ, and we define $\mathrm{W}^u_1(\mathbf{0}) \subset \mathrm{W}^u(\mathbf{0})$ as the unique one-dimensional strong unstable manifold associated with the single real eigenvalue of $\mathbf{0}$ in this case; we refer to the corresponding part of the (τ, σ)-plane with $\tau > 3\pi/2$ as Range II. In either case, determining the 'fate' of the one-dimensional (strong) unstable manifold $\mathrm{W}^u_1(\mathbf{0})$ is a natural choice for finding attractors of the infinite-dimensional DDE (1) because $\mathbf{0}$ is a relevant steady state of the system, and $\mathrm{W}^u_1(\mathbf{0})$ 'encodes' where nearby trajectories end up. We remark that this is also the case when there are additional complex conjugates unstable eigenvalues in Range II, because the strong unstable manifold then still converges to the (continuation of) the relevant attractor to which $\mathrm{W}^u(\mathbf{0})$ is attracted.

Because $\mathrm{W}^u_1(\mathbf{0})$ consists of two trajectories, it can be computed simply by numerical integration of the DDE from the initial function $x(t) = \mathbf{0} \pm \varepsilon e^{\lambda_{\mathbf{0}} t}$ with $0 < t < \max(\tau, \sigma)$, which lies in the unstable eigenspace of $\mathbf{0}$ at a sufficiently small initial distance ε from $\mathbf{0}$. Specifically, we set $\varepsilon = 10^{-5}$, integrate up to time $t = 1.5 \times 10^4$ and disregard transients to identify the respective bounded attractor. Figure 8 shows the result in the (τ, σ)-plane of this computation for a grid over the ranges $\tau = [0, 24]$ and $\sigma = [1, 4]$ in steps of 0.02 each. We find that the negative branch of $\mathrm{W}^u_1(\mathbf{0})$ grows beyond bound throughout. However, there are parameter regions where the positive branch of $\mathrm{W}^u_1(\mathbf{0})$ ends up at a bounded attractor. Below the line H^1_σ at $\sigma < \pi/2$ the equilibrium $\mathbf{0}$ is always stable and attracts $\mathrm{W}^u_1(\mathbf{0})$ for all $\tau > 0$. Above H^1_σ, we find a number of regions (shaded blue), where the positive branch of $\mathrm{W}^u_1(\mathbf{0})$ converges to a periodic, quasi-periodic or chaotic attractor; we call any such region an *attractor region* for short. In the complementary (white) part of the (τ, σ)-plane, both branches of $\mathrm{W}^u_1(\mathbf{0})$ show unbounded growth in amplitude.

We also show in Fig. 8 the relevant bifurcation curves that act as boundaries of the attractor regions. To the left of the Hopf bifurcation line H^1_τ is the curve $\mathrm{Hom}_{\mathbf{0}}$ of Shilnikov homoclinic, with its codimension-two point BP where $\mathrm{Hom}_{\mathbf{0}}$ changes from tame to wild. Near the point BP are the curves S_1 and PD_1 associated with the wild segment of $\mathrm{Hom}_{\mathbf{0}}$ discussed in Sec. 3.3. We find that the right boundary of this largest 'main' attractor region is formed by the curve PD_1 and the curve S, which emerges from the point GH and sharply turns at the cusp point C; note that, for clarity of the picture, we only show bifurcation curves above the line H^1_σ and in Range

I, that is, up to the line $\mathrm{H}^{\mathbf{1}}_{\tau}$. Near $\tau = 0$, a group of homoclinic curves Hom^n and saddle-node curves S^n bounds additional attractor regions, which become 'thinner' as σ increases, these new homoclinic curves accumulate on the curve $\mathrm{Hom}_{\mathbf{0}}$ and also approach the σ-axis. In Range II, for larger values of τ to the right of the line H^1_{τ}, we find further individual and similar attractor regions above H^1_{σ}, as well as a sequence of torus bifurcation curves T_n and saddle-node curves $\widetilde{\mathrm{S}}_n$ bounding them.

Figure 8 provides a 'summarizing view' of the structure of attractor regions in the (τ, σ)-plane. To detail specific properties of the different attractor regions and their bounding bifurcation curves, we discuss first the main attractor region in Range I, then the sequence of attractor regions near the σ-axis for small τ, and finally the repeating attractor regions for increasing τ.

4.1 The main attractor region in Range I

Figure 9 shows an enlargement of main attractor region in Range I in panel (a) and three examples of attractors in panels (b)–(d). Here, the coloring has been refined and now represents the periodicity of attractors. Specifically, Fig. 9(a) distinguishes attractors in terms of the number of local maxima of $x(t)$ per period, up to 10, as indicated by the color bar. Periodic time traces of attractors with more local maxima and those that have not been found to be periodic are not distinguished; the corresponding dynamics may be of high periodicity, quasiperiodic or chaotic. The main attractor region lies above the curve H^1_{σ}, from which a basic periodic orbit with a single local maximum per period bifurcates. Figure 9(b) illustrates how the one-dimensional manifold $\mathrm{W}^u_1(\mathbf{0})$ converges to the basic periodic orbit, which exists in a large sub-region of the (τ, σ)-plane. It is bounded above, for increasing σ, by the segment of the curve $\mathrm{Hom}_{\mathbf{0}}$ to the left of the Belyakov point BP. For larger values of τ, however, there is a sequence of period doublings, starting with the curve PD_1 that we found near the wild segment of $\mathrm{Hom}_{\mathbf{0}}$ to the right of BP; see Sec. 3.3. Fig. 9(c) shows how $\mathrm{W}^u_1(\mathbf{0})$ converges to a period-doubled periodic orbit that bifurcates from PD_1. The accumulation of further curves of period-doubling bifurcations (not shown in panel (a)) in a peridod-doubling cascade results in a sub-region where $\mathrm{W}^u_1(\mathbf{0})$ lies in the basin of a chaotic attractor; an example is shown in panel (d).

Overall, we find that the main attractor region in the (τ, σ)-plane of Fig. 9(a) is bounded by a segment of the curve S emerging from the point GH_1, as well as by segments of the bifurcation curves $\mathrm{Hom}_{\mathbf{0}}$, PD_1, and S_2 that are associated with the wild case of Shilnikov bifurcation. We remark that the top-right part of the attractor region with chaotic or high-period attractors is not clearly delineated by the curves S_1 and S_2 alone; here, we find the disappearance of the chaotic attractor in (different kinds of) boundary crises [19, 35].

4.2 Sequence of attractor regions in Range I

Figure 9(a) also shows the second attractor region near the σ-axis. It is bounded by homoclinic curves Hom^1 and Hom^2 at bottom and top, and by a saddle-node bifurcation curve S^1 to the right; hence, this second attractor region has a 'simpler structure' compared to the main attractor region. Moreover, except for very near S^1, we find here an attracting periodic orbit with a single local maximum; and similarly for the third and further attractor regions near the σ-axis.

Figure 10 illustrates that the second attractor region marks the start of an infinite sequence as σ increases; as in Fig. 8(a), we do not distinguish the number of local maxima here. The relevant part of the (τ, σ)-plane in Range I for small τ in Fig. 10(a) shows that each successive attractor region is similarly bounded by further curves Hom^n and S^n. Along each of the shown curves Hom^n one finds a tame Shilnikov homoclinic bifurcation since the saddle quantity of equilibrium $\mathbf{0}$ is negative here (it only changes sign at $\tau \approx 1.97$, beyond the range shown); see Sec. 3.3. Dashing in Fig. 10(a) indicates segments of curves that could not be continued directly, but whose locations have been verified indirectly and are shown for reference. The issue

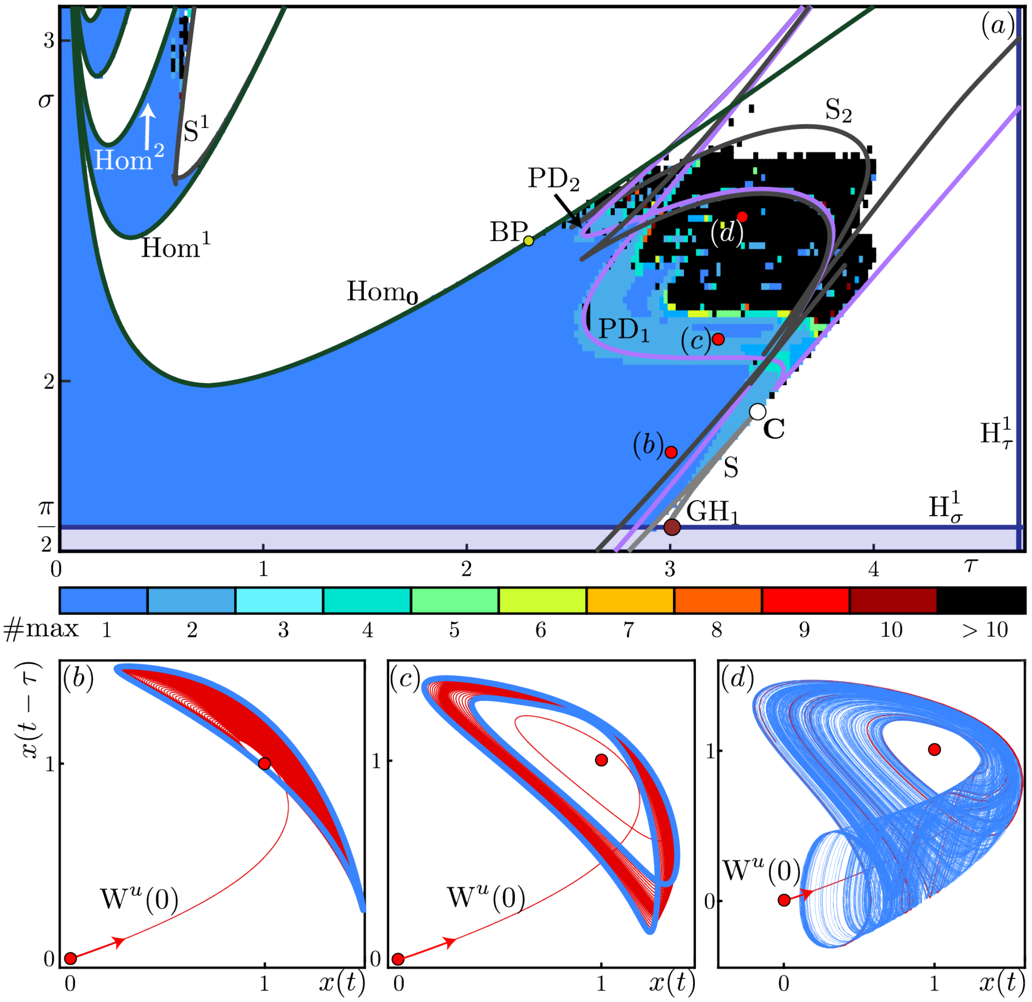

Figure 9: The main attractor region in Range I and example attractors. Panel (a) shows the relevant part of the (τ, σ)-plane with coloring by the number of local maxima per period as indicated by the color bar; also shown are the boundary curves H^1_σ, $\mathrm{Hom}_{\mathbf{0}}$, S, S_1, and PD_1 with their corresponding codimension-two points, as well as curves Hom^1, Hom^2, and S^1 of the upper left attractor region. Panels (b) to (d) show projections onto the $(x(t), x(t-\tau))$-plane of the attractors (blue) approached by the one-dimensional unstable manifold $\mathrm{W}^u_1(\mathbf{0})$ (red) for $(\tau, \sigma) = (3, 1.6)$, $(3.2, 2.1)$ and $(3.3, 2.6)$, respectively; these parameter points are marked in panel (a).

is that the continuation of bifurcation curves becomes very challenging in light of the increasing complexity of nearby orbits as the value of σ increases.

Observe in Fig. 10(a) the self-similar structure of repeating and accumulating attractor regions that decrease in size and approach the σ-axis with increasing σ. The curve $\mathrm{Hom}_{\mathbf{0}}$ at the bottom is the upper boundary of the main attractor region discussed in Sec. 4.1. Near the righ-hand boundary S^1 of the second attractor region we find a curve PD^1 of a first period-doubling bifurcation of a cascade, which generates a small sub-region of chaotic dynamics; the chaotic attractor at the marked parameter point is shown in panel (b). This bifurcation structure repeats for increasing σ; however, for $n \geq 2$ the curve PD^n is already extremely close to the curve S^n where the respective chaotic attractor disappears, meaning that the region with chaotic dynamics is impractically small. Figure 10 clearly shows an important property of the DDE (1): the bounding curves Hom^n of successive attractor regions accumulate rapidly on the σ-axis

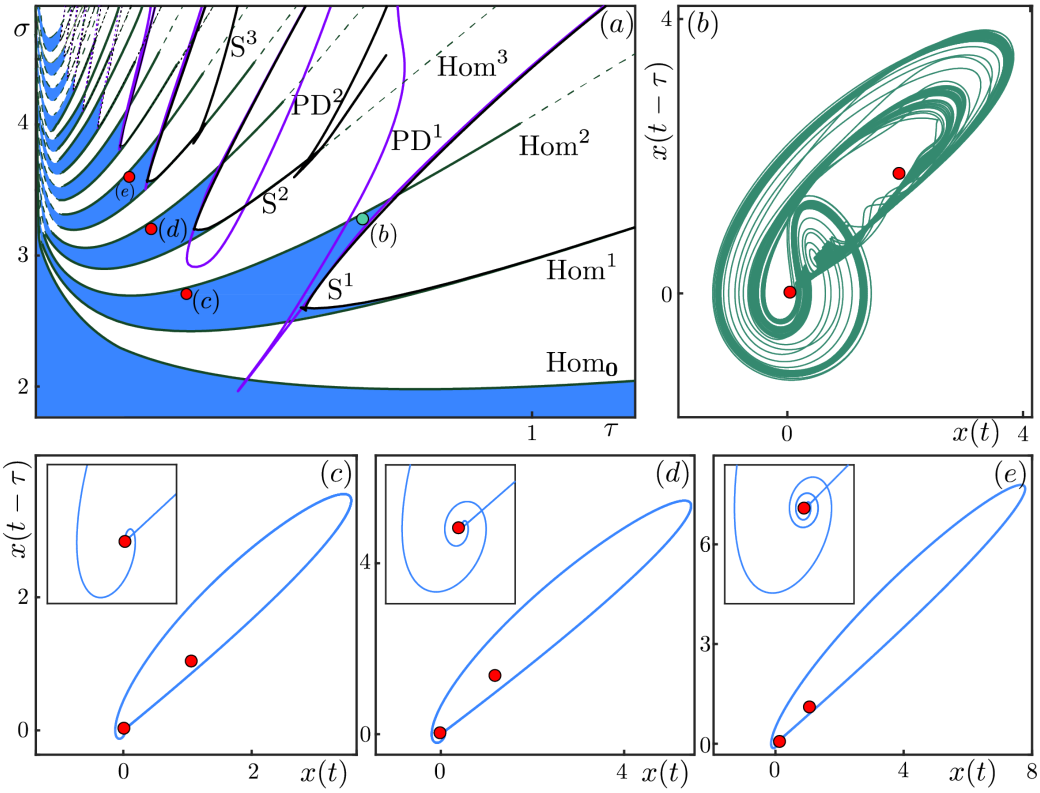

Figure 10: Sequence of attractor regions (blue) in Range I near $\tau = 0$ and example attractors. Panel (a) shows the relevant part of the (τ, σ)-plane with the boundary curves $\mathrm{Hom}_{\mathbf{0}}$, Hom^n and S^n; dashed segments of bifurcation curves could not be continued directly and are included for reference. Panels (b) to (e) show projections onto the $(x(t), x(t - \tau))$-plane of the chaotic attractor at $(\tau, \sigma) = (0.62, 3.14)$, and of the attracting periodic orbit at $(\tau, \sigma) = (0.3, 2.68)$, $(0.26, 3.18)$, and $(0.2, 3.5)$, respectively; these parameter points are marked in panel (a).

and, hence, also on each other. Panels (c) to (e) show the attracting periodic orbits at the marked parameter points in panel (a), which are all in a 'similar position' in the second, third and fourth attractor region, near the homoclinic bifurcation curves Hom^2, Hom^4 and Hom^6, respectively. From attractor region to attractor region, the size of the periodic orbit grows; notice the differences in scale in panels (c)–(e). Moreover, as the insets show, the periodic orbit features increasingly more spiraling near the equilibrium $\mathbf{0}$.

Figure 10 illustrates that the second delay τ of the NAS2F model (1) 'reveals' the homoclinic bifurcation $\mathrm{Hom}_{\mathbf{0}}$, as well as the infinitely many further homoclinic bifurcations Hom^n, which are 'unavailable' to the Hutchinson-Wright equation with $\tau = 0$ [23, 49]. For any fixed value of σ, even small values of τ lead to the appearance of many attracting periodic and homoclinic orbits, and their number increases beyond any bound as σ increases. Hence, introducing a small delay τ into the Hutchinson-Wright equation can be seen as revealing or unfolding this complexity.

4.3 Repeating attractor regions in Range II

Figure 11 shows the first attractor region in Range II of the (τ, σ)-plane, which lies between the lines H^1_σ and H^2_σ of Hopf bifurcation. Here, the unstable equilibrium $\mathbf{1}$ has three unstable eigenvalues, the strongest real one and a pair of complex conjugate ones. In spite of the larger

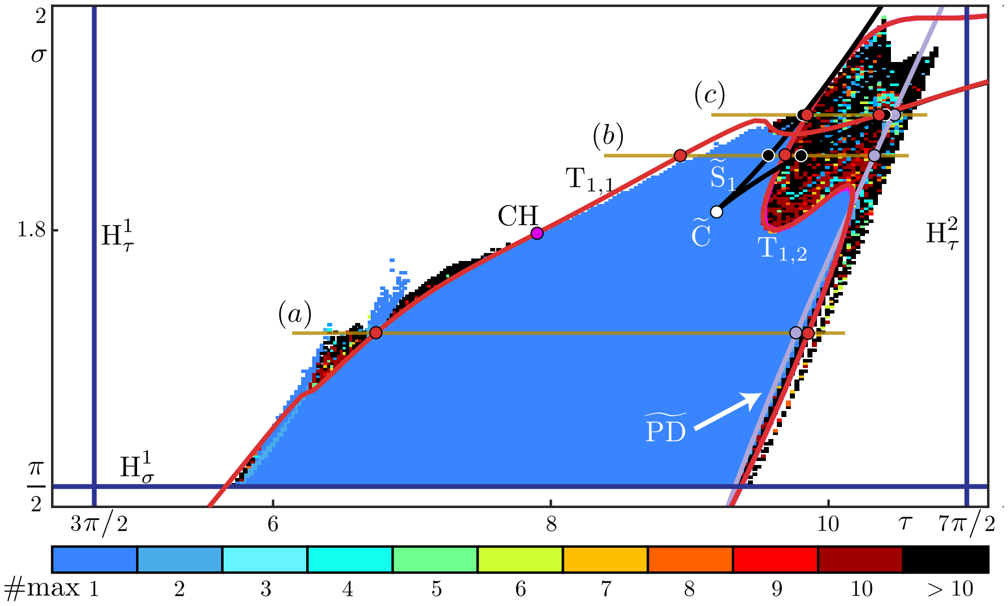

Figure 11: The first attractor region in Range II of the (τ, σ)-plane, with coloring by the number of local maxima per period as indicated by the color bar; also shown are the boundary curves $\mathrm{T}_{1,1}$ and $\mathrm{T}_{1,2}$ (red) of torus, $\widetilde{\mathrm{S}}_1$ (black) of saddle-node, and $\widetilde{\mathrm{PD}}$ (light purple) of period-doubling bifurcations. The one-parameter bifurcation diagrams along the three horizontal segments (golden) are presented in Figure 12.

dimension of the unstable manifold, the one-dimensional strong manifold $\mathrm{W}^u_1(\mathbf{0})$ still reliably 'picks up' attractors, which we color again by periodicity of the orbits as given by up to ten local maxima. To account for the smaller range in the σ-direction, its stepsize was reduced to 0.002, while maintaining the stepsize of 0.02 in the τ-direction. The large region of basic periodic orbits with a single maximum emerging from H^1_σ is delimited by the curves $\mathrm{T}_{1,1}$ on the left and $\mathrm{T}_{1,2}$ on the right/top. We also show two additional bifurcations curves: a saddle-node curve $\widetilde{\mathrm{S}}_1$ with its codimension-two cusp point $\widetilde{\mathrm{C}}$, where it sharply turns and then aligns with $\mathrm{T}_{1,1}$, and the period-doubling curve $\widetilde{\mathrm{PD}}$, which lies near the curve $\mathrm{T}_{1,2}$.

The left boundary of the attractor region in Fig. 11 is effectively formed by the torus bifurcation curve $\mathrm{T}_{1,1}$. This curve effectively bounds the large sub-region above the line H^1_σ of the basic periodic orbit, and it has a change of criticality at a codimension-two point CH at $\tau = 7.76$, known as Chenciner point [9, 25]. Below the point CH the curve $\mathrm{T}_{1,1}$ is supercritical and stable tori exist to its left; this is indicated by attractors of different periodicities, and we do not compute and show the boundaries of associated resonance tongues. Above the point CH the curve $\mathrm{T}_{1,1}$ is subcritical, an unstable torus emerges to its right and $\mathrm{W}^u_1(\mathbf{0})$ does not converge to a finite attractor. The unstable torus coexists with a stable torus and both disappear a bit to the right of the curve $\mathrm{T}_{1,1}$ in a fashion similar to a saddle-node bifurcation of periodic solutions; however, this involves a loss of normal hyperbolicity and break-up of the tori near where they disappear. To the right of this 'fold of tori', $\mathrm{W}^u_1(\mathbf{0})$ converges to the basic periodic orbit. Near its maximum at $\tau \approx 1.89$, the curve $\mathrm{T}_{1,1}$ ceases to play a role for the boundary for the attractor region. Along the curve $\widetilde{\mathrm{PD}}$, which runs parallel to $\mathrm{T}_{1,2}$ up to $\tau \approx 1.8$, the basic period-one attractor loses stability and a stable period-two attractor emerges, which loses stability at the torus bifurcation curve $\mathrm{T}_{1,2}$. Past its crossing point with $\widetilde{\mathrm{PD}}$, the S-shaped curve $\mathrm{T}_{1,2}$ marks the boundary where the period-one orbit vanishes. The curve $\mathrm{T}_{1,2}$ is supercritical throughout, with stable tori existing to its right and top, with a consideably larger sub-region of attractors

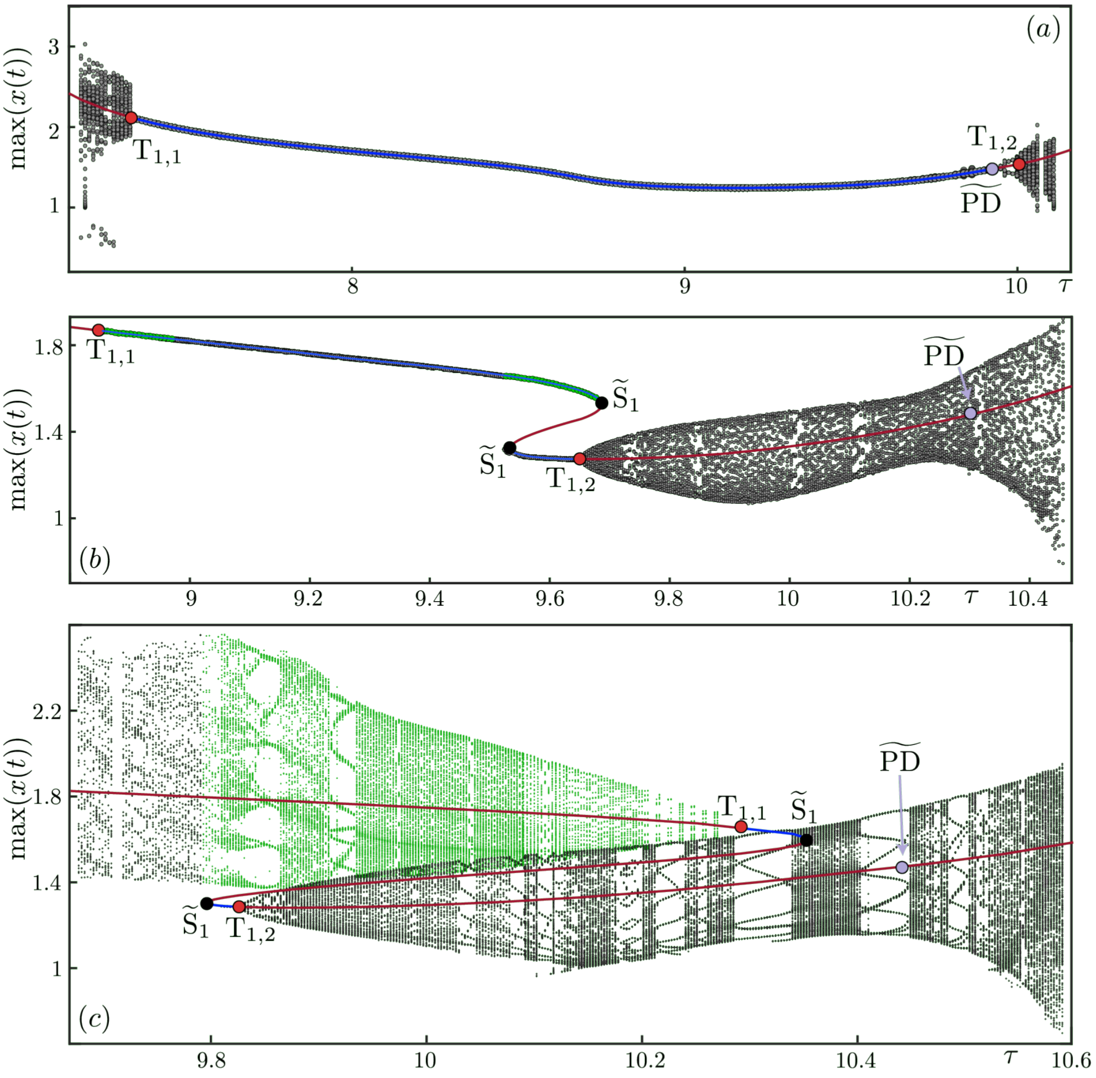

Figure 12: One-parameter bifurcation diagrams in τ along the horizontal sections for $\sigma = 1.76$ (a), $\sigma = 1.86$ (b) and $\sigma = 1.9$ (c) that are indicated in Fig. 11. Shown are the local maxima of $x(t)$ of the respective attractor, as obtained from $W_1^u(\mathbf{0})$ (black dots), by paramter sweeping (green dots), and by numerical continuation of the basic periodic orbit (blue when stable, red when unstable); also shown are the bifurcation points $T_{1,1}$ and $T_{1,2}$ (red), $\widetilde{PD}$ (light purple) and $\widetilde{S}_1$ (black).

of high periodicity. Thes attractors may be chaotic and appear or disappear in boundary crisis bifurcations. The curve $\widetilde{S}_1$ at the top of Fig. 11 is associated with a region of bistability, as we discuss next.

We now illustrate in Fig. 12 the complexity of the observed dynamics in the attractor region in Fig. 11 by showing one-parameter bifurcation diagrams in τ along the three shown horizontal lines. For each such section, we show the local maxima of $x(t)$ of the respective attractor, obtained in three different ways: underlying each image are the branches of the basic periodic orbit with a single local maximum, which we obtain by continuation; moreover, we show the attractor as obtained from computing $W_1^u(\mathbf{0})$, as well as the 'missing' attractor (not obtained from $W_1^u(\mathbf{0})$) in regions of bistability; the latter is obtained by 'parameter sweeping' in τ from already determined nearby attractors.

Figure 12(a) shows the one-parameter bifurcation diagram for $\sigma = 1.76$. Here, the basic periodic orbit is stable between the point $\mathrm{T}_{1,1}$ of torus bifurcation and the point $\widetilde{\mathrm{PD}}$ of period-doubling bifurcation, and it attracts $\mathrm{W}^u_1(\mathbf{0})$ throughout this τ-range. To the left of $\mathrm{T}_{1,1}$, we find a transition to an attracting torus with high-period or quasiperiodic dynamics, which then suddenly disappears at $\tau \approx 7.18$ in a boundary crisis, seemingly after breaking up and generating chaotic dynamics. Similarly, to the right of $\widetilde{\mathrm{PD}}$, there is a τ-range with a stable period-doubled periodic orbit, which then undergoes a torus bifurcation at $\mathrm{T}_{1,2}$. The bifurcating attracting torus also disappears suddenly in a boundary crisis at $\tau \approx 10.12$; moreover, in the small τ-range $[10.06, 10.08]$ we do not detect a finite attractor, which is likely due to a 'channel' formed by further boundary crisis bifurcations as discussed in [35].

In the one-parameter bifurcation diagram for $\sigma = 1.86$ in Fig. 12(b), the periodic orbit branch obtained by continuation features a τ-range of bistability between the two points of saddle-node bifurcations labelled $\widetilde{\mathrm{S}}_1$. The 'hidden' attractor that is not reached by $\mathrm{W}^u_1(\mathbf{0})$ here is the stable periodic orbit with the larger maximum. Hence, there is a sudden switch at the left point $\widetilde{\mathrm{S}}_1$ of $\mathrm{W}^u_1(\mathbf{0})$ to the periodic orbit with lower maximum. Notice that the upper branch of stable periodic orbits is also not reached by $\mathrm{W}^u_1(\mathbf{0})$ for $\tau < 9.5$, well to the right of the point $\mathrm{T}_{1,1}$. This is due to the subcritical nature of this torus bifurcation, which is now encountered at a much larger value of τ; compare with Fig. 11. A new feature of Fig. 12(b) is also the swapping of positions of the points $\mathrm{T}_{1,2}$ and $\widetilde{\mathrm{PD}}$, resulting in a larger τ-range with an attracting torus. The dynamics on the torus is still largely of high period or quasiperiodic, but with some hints of periodic windows.

Figure 12(c) shows the one-parameter bifurcation diagram for $\sigma = 1.9$, where the torus bifurcation point $\mathrm{T}_{1,1}$ is supercritical again; moreover, this point is now near the right-most saddle-node bifurcation point $\widetilde{\mathrm{S}}_1$, well past the left-most point $\widetilde{\mathrm{S}}_1$. As a result, the attracting torus bifurcating from $\mathrm{T}_{1,1}$ is reachable by $\mathrm{W}^u_1(\mathbf{0})$, but only to the left of the left-most point $\widetilde{\mathrm{S}}_1$. At this saddle-node bifurcation of the periodic orbits, $\mathrm{W}^u_1(\mathbf{0})$ switches to lying in the basin of the emerging periodic orbit with the lower maximum, which undegoes the torus bifurcation $\mathrm{T}_{1,2}$. To the right of this point, $\mathrm{W}^u_1(\mathbf{0})$ ends up at the bifurcating attracting torus. Overall, we find a τ-range of bistability, still between the two points $\widetilde{\mathrm{S}}_1$, but now mostly between two attracting tori in between the points $\mathrm{T}_{1,2}$ and $\mathrm{T}_{1,1}$. Due to the smaller overall τ-range of Figure 12(c), the dynamics on either torus shows clear τ-ranges where one finds locked periodic orbits of quite low periods. These correspond to and explain the differently colored dots in the bifurcation diagram of Fig. 11, where a complicated mix of different periodicities is observed to the right of the curve $\mathrm{T}_{1,2}$.

As was already clear from Fig. 8, one finds a sequence of further attractor regions above the line H^1_σ as τ is increased. Figure. 13 shows the first three such attractor regions in Range II: the one from Fig. 11 and two more, which each lie in between successive vertical lines H^n_τ. The crossing of each such Hopf bifurcation curve enlarges the dimension of the unstable manifold of the equilibrium 0 by two; nevertheless, the one-dimensional strong manifold W^u_1 remains a reliable 'tool' to identify the existence of nontrivial attractors; they are shown in Fig. 13 in terms of the number of detected local maxima per period. The second and third attractor region have a similar structure, with torus bifurcation curves $\mathrm{T}_{n,1}$ on the left and $\mathrm{T}_{n,2}$ on the right bounding a large sub-region of a basic attracting periodic solution (with a single maximum). In contrast to the first attractor region highlighted in Fig. 11, these further torus bifurcation curves do not have changes of criticality: the bifurcating tori are consistently stable and to the 'outside' of the large sub-region of a basic periodic orbits, leading in Fig. 13 to a 'surrounding' region with quasiperiodic or high-period dynamics. Notice also that the second and third attractor regions do not have period-doubling curves; instead, we find torus bifurcation curves $\mathrm{T}_{n,3}$ in corresponding locations. The attractor regions 'shrink' in size with increasing τ, with the sub-regions of period-one attractors becoming yet smaller. Nevertheless, a common feature remains

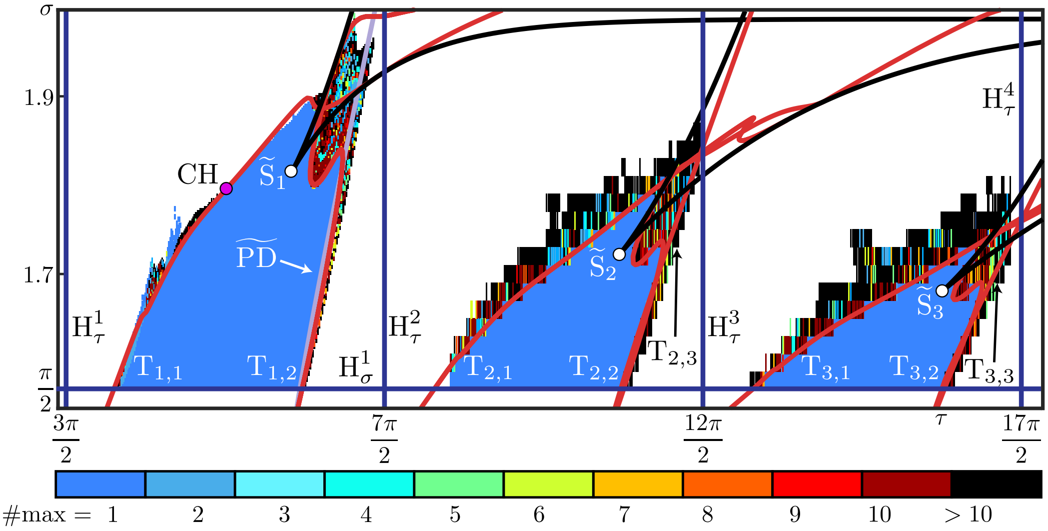

Figure 13: The first three attractor regions in Range II of the (τ,σ)-plane for larger τ; compare with Figs. 8 and 11.

the existence of a curve $\widetilde{\mathrm{S}}_n$ of saddle-node bifurcation with a cusp point $\widetilde{\mathrm{C}}_n$ and associated τ-ranges of bistability.

5 Discussion and outlook

Our central object of study is Eq. (1), a DDE that depends only on two parameters, which are the (rescaled) delays of the main feedbacks loops in the AMOC. The formulation of Eq. (1) arises from the idea of representing the two independent feedback loops of the AMOC as 'isolated' or independent processes. The larger delay τ represents the advective feedback associated with the exchange of heat and salinity by the AMOC. The second delay σ is associated with the vertical mixing of polar waters due to convection. From the application point of view, τ is much larger than σ and, hence, this paramter regime is where the physically relevant dynamics occurs.

We focused here on the case of the NAS2F model without external forcing, when it takes the form of Eq. (1) with the two (rescaled) delays τ and σ as its only parameters. This DDE can be regarded as a basic conceptual model designed to understand AMOC dynamics due to the feedback processes without external influences. The key new aspect is that the two feedback loops interact in a multiplicative way, and Eq. (1) can also be seen as a basic model for any systems where two independent feedbacks interact in this 'unusual' way. More specifically, the NAS2F model takes the form of the logistic equation with two independent delays and, in this way, provides a 'natural unfolding' of the Hutchinson-Wright equation with an additional independent delay. This is of general interest because this well-known equation is among the first examples to demonstrate the richer nature of solutions that DDEs can exhibit, compared to their ODE counterparts.

Despite the simple looking form of Eq. (1), our bifurcation analysis revealed an intruiging structure of bifurcations in the (τ,σ)-plane with a wide variety of observable dynamics. Starting from the equilibrium solution **1**, which is stable for sufficiently low σ, we find that oscillations arise along supercritical segments of Hopf bifurcation. The bifurcating stable oscillating solutions are subject to nonlinear interactions: they become pulse-like and/or undergo Shilnikov, period-doubling and torus bifurcations, either of which may lead to observable chaotic dynamics. As organizing centers of the bifurcation diagram in the (τ,σ)-plane we identified a Belyakov point (where the Shilnikov bifurcation becomes 'wild') and a T-point bifurcation, where two distinctive homoclinic orbits 'merge' into a heteroclinic cycle; the latter codimension-two bifurcation has not been found previously in a DDE to the best of our knowledge.

We complemented the direct continuation of different types of solutions and their bifurcations with determining where in the (τ, σ)-plane one finds relevant attractors of Eq. (1). This is a particular challenge for DDEs in light of their infinite-dimensional nature, and the key is to consider the fate of a well-defined invariant object. In our case, we compute the (strong) one-dimensional unstable manifold of the saddle equilibrium $\mathbf{0}$ by starting numerical integrations from the associated eigenfunction of the linearized system. This is a natural and practical choice because this equilibrium represents one of the states of the AMOC; in particular, $\mathbf{0}$ is involved in global bifurcations that change the nature of attractors, and its stable manifold may separate different basins of attraction.

In this way, we found a main attractor region in the (τ, σ)-plane, as well as sequences of further attractor regions along both the σ-axis and the τ-axis; moreover, we were able to characterize how different bifurcation curves bound them. The repeating attractor regions for increasing σ and low values of τ are bounded by homoclinic bifurcation curves, all of Shilnikov type, which accumulate on the σ axis. This explains their disappearance in the limit $\tau = 0$, where Eq. (1) becomes the (one-delay) Hutchinson-Wright equation. In effect, all this complex dynamics is not present in the Hutchinson-Wright equation, but any small increase in τ causes it to 'reveal itself'. The relevant sequence of attractor regions from the climate modelling perspective, however, is the one for increasing τ and low values of σ, where the delay of advective feedback loop is larger than that of the convective one. These attractor regions effectively consist of a main region with stable oscillations, which destabilize at curves of torus bifurcations leading to dynamics on attracting tori that may be quasiperiodic or locked. As a further relevant feature we found considerable sub-regions of bistability that are bounded by a saddle-node bifurcation curve with a cusp point. Our estimates for the rescaled delay times τ and σ indicate that these attractor regions lie within a physically meaningful parameter range.

Despite being a relatively simple phenomenological model, the NAS2F model (1) captures interesting aspects of the interaction between the two main feedback loops of the AMOC. It exhibits far richer dynamics than expected from its simple form and, in this way, showcases the ability of delay differential equations to 'encode' complex dynamics in a compact form that is ameanable to analysis with advanced tools from dynamical systems. Moreover, due to its direct connection with the doubly-delayed logistic and Hutchinson-Wright equations, we hope that Eq. (1) will be of interest beyond climate science.

Returning to the context of climate modelling, there are several directions for future research. Firstly, Eq. (1) could be made more 'realistic' even at the conceptual level by considering other effects, particularly, external influences via the forcing component included in Eq. (2). A first natural step is to study constant forcing representing the average freshwater inflow into the North Atlantic. Even this simple addition has the potential to alter the dynamics of Eq. (1) significantly, but we do not expect the attractor regions to disappear entirely. From the modelling perspective, it is also important to consider the impact of seasonal variations on the AMOC by introducing periodic forcing around an average value of constant fresh water influx. The analysis of the resulting periodically forced NAS2F DDE model would constitute an interesting and substantial project in its own right.

Secondly, the NAS2F model offers interesting qualitative insights, but direct comparison with more complex models or even data is challenging. We presented here estimates for ranges of the two delays. While this showed that attractor regions we found lie in plausable parameter region, it simultaneaoulsy demonstrates the difficulty of determining values of parameters of conceptul models. Nevertheless, attempting such comparisons, initially with more manageable intermediate models, would be of interest. In this regard we mention that the modelling approach of including explicit delayed terms could also be used to 'calibrate' models by 'matching' similar types of dynamics observed in different models. Moreover, there is the possibility to enhance intermediate models by modelling feedback loops in a similar way, either to improve the models efficiency in simulations, or to incorporate feedback effects that have not yet been included.

Finally, the introduction of explicit delayed terms into box models, such as those of Stommel and Welander [42, 48] and variations [1, 32] opens perspectives for the investigation of the AMOC, as well as other global climate phenomena; investigations in this direction are ongoing. In this context we note that DDEs were first introduced and studied as conceptual models of the El Niño Southern Oscillation (ENSO) [17, 24, 27, 43, 50]. The underlying idea or paradigm is the so-called delayed action oscillator description of ENSO, where perturbations of the thermocline off the coast of Peru are transported by Rossby and Kelvin waves across the Pacific Ocean to generate a delayed feedback loop. While most DDE models in climate dynamics are of a phenomonological nature, it is important to realise that delay equations can be derived more rigorously as reduction of more complicated models described by partial differential equations; an example of such a derivation can be found in [14].

Acknowledgements

We thank Tra Dinh and Priya Subramanian for helpful discussions. The research of R.M and B.K was supported by Royal Society Te Apārangi Marsden Fund grant #19-UOA-223, and that of S.R. by UKRI Grant No. EP/Y027531/1.

References

[1] J. Bailie, H. A. Dijkstra, and B. Krauskopf. A detailed analysis of the origin of deep-decoupling oscillations. *Chaos*, 35(7):73126, 2025.

[2] L. A. Belyakov. Bifurcation of systems with homoclinic curve of a saddle-focus with saddle quantity zero. *Mathematical notes of the Academy of Sciences of the USSR*, 36(5):838–843, 1984.

[3] P. Bogacki and L. F. Shampine. A 3(2) pair of Runge-Kutta formulas. *Applied Mathematics Letters*, 2(4):321–325, 1989.

[4] C. A. Boulton, L. C. Allison, and T. M. Lenton. Early warning signals of Atlantic Meridional Overturning Circulation collapse in a fully coupled climate model. *Nature Communications*, 5(1):1–9, 2014.

[5] R. D. Braddock and P. Van den Driessche. On a two lag differential delay equation. *The ANZIAM Journal*, 24(3):292–317, 1983.

[6] H. L. Bryden and S. Imawaki. Ocean heat transport. *International Geophysics*, 77:455–474, 2001.

[7] V. Bykov. On systems with separatrix contour containing two saddle-foci. *Journal of Mathematical Sciences*, 95(5):2513–2522, 2001.

[8] P. Cessi. A simple box model of stochastically forced thermohaline flow. *Journal of Physical Oceanography*, 24(9):1911–1920, 1994.

[9] A. Chenciner. Bifurcations de points fixes elliptiques. *Publications Mathmatiques de l'IHÉS*, 66(1):5–91, 1987.

[10] J. L. Creaser, B. Krauskopf, and H. M. Osinga. α-flips and T-points in the Lorenz system. *Nonlinearity*, 28(3):R39–R65, 2015.

[11] H. A. Dijkstra. The role of conceptual models in climate research. *Physica D: Nonlinear Phenomena*, 457:133984, 2024.

[12] R. D. Driver. *Ordinary and delay differential equations.* Springer Science & Business Media, 2012.

[13] K. Engelborghs, T. Luzyanina, and D. Roose. Numerical bifurcation analysis of delay differential equations using DDE-BIFTOOL. *ACM Transactions on Mathematical Software*, 28(1):1–21, 2002.

[14] S. K. Falkena, C. Quinn, J. Sieber, and H. A. Dijkstra. A delay equation model for the Atlantic Multidecadal Oscillation. *Proceedings of the Royal Society A*, 477(2246):20200659, 2021.

[15] C. K. Folland, A. W. Colman, D. P. Rowell, and M. K. Davey. Predictability of northeast Brazil rainfall and real-time forecast skill, 1987-98. *Journal of Climate*, 14(9):1937–1958, 2001.

[16] A. C. Fowler. An asymptotic analysis of the delayed logistic equation when the delay is large. *IMA Journal of Applied Mathematics*, 28(1):41–49, 1982.

[17] M. Ghil, I. Zaliapin, and S. Thompson. A delay differential model of ENSO variability: parametric instability and the distribution of extremes. *Nonlinear Processes in Geophysics*, 15(3):417–433, 2008.

[18] P. Glendinning and C. Sparrow. T-points: a codimension two heteroclinic bifurcation. *Journal of Statistical Physics*, 43(3):479–488, 1986.

[19] C. Grebogi, E. Ott, and J. Yorke. Crises, sudden changes in chaotic attractors, and transient chaos. *Physica D*, 7:181200, 1983.

[20] K. Green and B. Krauskopf. A two-parameter study of the locking region of a semiconductor laser subject to phase-conjugate feedback. *SIAM Journal on Applied Dynamical Systems*, 2(2):254–276, 2003.

[21] S. Guo and J. Wu. *Bifurcation theory of functional differential equations.* Springer Science & Business Media, 2013.

[22] J. K. Hale and S. M. Verduyn Lunel. *Introduction to functional differential equationss.* Springer Science & Business Media, 2013.

[23] G. E. Hutchinson. Circular causal systems in ecology. *Ann. NY Acad. Sci*, 50(4):221–246, 1948.

[24] H. Kaper and H. Engler. *Mathematics and climate.* Society for Industrial and Applied Mathematics, 2013.

[25] A. Keane and B. Krauskopf. Chenciner bubbles and torus break-up in a periodically forced delay differential equation. *Nonlinearity*, 31(6):165–187, 2018.

[26] A. Keane, B. Krauskopf, and C. M. Postlethwaite. Investigating irregular behavior in a model for the El Niño Southern Oscillation with positive and negative delayed feedback. *SIAM Journal on Applied Dynamical Systems*, 15(3):1656–1689, 2016.

[27] A. Keane, B. Krauskopf, and C. M. Postlethwaite. Climate models with delay differential equations. *Chaos: An Interdisciplinary Journal of Nonlinear Science*, 27(11):114309, 2017.

[28] Y. A. Kuznetsov. *Elements of applied bifurcation theory.* Springer Science & Business Media, 1998.

[29] S. Levitus, R. Burgett, and T. P. Boyer. *World Ocean Atlas 1994. Vol. 3, Salinity.* U.S. Department of Commerce, 1994.

[30] X. Li, S. Ruan, and J. Wei. Stability and bifurcation in delay-differential equations with two delays. *Journal of Mathematical Analysis and Applications*, 236(2):254–280, 1999.

[31] M. S. Lozier, F. Li, S. Bacon, F. Bahr, A. S. Bower, S. A. Cunningham, M. F. De Jong, L. De Steur, B. DeYoung, J. Fischer, S. F. Gary, B. J. Greenan, N. P. Holliday, A. Houk, L. Houpert, M. E. Inall, W. E. Johns, H. L. Johnson, C. Johnson, J. Karstensen, G. Koman, I. A. Le Bras, X. Lin, N. Mackay, D. P. Marshall, H. Mercier, M. Oltmanns, R. S. Pickart, A. L. Ramsey, D. Rayner, F. Straneo, V. Thierry, D. J. Torres, R. G. Williams, C. Wilson, J. Yang, I. Yashayaev, and J. Zhao. A sea change in our view of overturning in the subpolar North Atlantic. *Science*, 363(6426):516–521, 2019.

[32] A. Neff, A. Keane, H. Dijkstra, and B. Krauskopf. Bifurcation analysis of a North Atlantic Ocean box model with two deep-water formation sites. *Physica D*, 456:133907, 2023.

[33] R. D. Nussbaum. *Differential-delay equations with two time lags.* American Mathematical Soc, 1978.

[34] M. J. Piotrowska and M. Bodnar. Logistic equation with treatment function and discrete delays. *Mathematical Population Studies*, 21(3):166–183, 2014.

[35] J. Rankin and H. M. Osinga. Parameter-dependent behaviour of periodic channels in a locus of boundary crisis. *The European Physical Journal Special Topics*, 226:1739–1750, 2017.

[36] J. Robson, K. Lohmann, D. Smith, and M. D. Palmer. Causes of the rapid warming of the North Atlantic Ocean in the mid-1990s. *Journal of Climate*, 25(12):4116–4134, 2012.

[37] D. P. Rowell, C. K. Folland, K. Maskell, and M. N. Ward. Variability of summer rainfall over tropical North Africa (1906-92): Observations and modelling. *Meteorol. Soc*, 121(66):669–704, 1994.

[38] R. Schuster and H. Schuster. Reconstruction models for the Ehrlich ascites tumor of the mouse. *Mathematical population dynamics*, 2:335–348, 1995.

[39] L. P. Shilnikov. A case of the existence of a countable number of periodic motion. *In Sov. Math. Dokl*, 6:163–166, 1965.

[40] J. Sieber, K. Engelborghs, T. Luzyanina, G. Samaey, and D. Roose. DDE-BIFTOOL manual - Bifurcation analysis of delay differential equations. *arXiv*, 1406.7144, 2014.

[41] H. L. Smith. *An introduction to delay differential equations with applications to the life sciences.* Springer Science & Business Media, 2011.

[42] H. Stommel. Thermohaline convection with two stable regimes of flow. *Tellus*, 13(2):224–230, 1961.

[43] M. J. Suarez and P. S. Schopf. A delayed action oscillator for ENSO. *Journal of Atmospheric Sciences*, 45(21):3283–3287, 1988.

[44] R. T. Sutton and B. Dong. Atlantic Ocean influence on a shift in European climate in the 1990s. *Nature Geoscience*, 5(11):788–792, 2012.

[45] R. T. Sutton and D. L. Hodson. Atlantic Ocean forcing of North American and European summer climate. *Science*, 309(5731):115–118, 2005.

[46] E. Vanderborght, R. M. van Westen, and H. A. Dijkstra. Feedback processes causing an AMOC collapse in the Community Earth System Model. *Journal of Climate*, 5083-5102, 2025.

[47] C. Wang and S. K. Lee. Co-variability of tropical cyclones in the North Atlantic and the eastern North Pacific. *Geophysical Research Letters*, 36(24), 2009.

[48] P. Welander. A simple heat-salt oscillator. *Dynamics of Atmospheres and Oceans*, 6(4):233–242, 1982.

[49] M. Wright. A non-linear difference-difierential equation. *J. Reine Angew. Math*, 194:66–87, 1955.

[50] I. Zaliapin and M. Ghil. A delay differential model of ENSO variability – Part 2: Phase locking, multiple solutions and dynamics of extrema. *Nonlinear Processes in Geophysics*, 17(2):123–135, 2010.